Feasibility evaluation for development of composite propellers with embedded piezoelectric sensors

Huijer, Arnaud; Zhang, Xiaobo; Kassapoglou, Christos; Pahlavan, Lotfollah

DOI
10.1016/j.marstruc.2022.103231

Publication date
2022

Document Version
Final published version

Published in
Marine Structures

Citation (APA)
Huijer, A., Zhang, X., Kassapoglou, C., & Pahlavan, L. (2022). Feasibility evaluation for development of composite propellers with embedded piezoelectric sensors. *Marine Structures*, *84*, Article 103231. https://doi.org/10.1016/j.marstruc.2022.103231

Marine Structures 84 (2022) 103231

Contents lists available at ScienceDirect

Marine Structures

journal homepage: www.elsevier.com/locate/marstruc

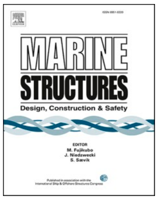

Feasibility evaluation for development of composite propellers with embedded piezoelectric sensors

Arnaud Huijer [a,*], Xiaobo Zhang [a], Christos Kassapoglou [b], Lotfollah Pahlavan [a]

[a] Faculty of Mechanical, Maritime, and Materials Engineering, Delft University of Technology, Mekelweg 2, 2628AX, Delft, the Netherlands
[b] Faculty of Aerospace Engineering, Delft University of Technology, Kluyverweg 1, 2629HS, Delft, the Netherlands

ARTICLE INFO

Keywords:
Composite marine propeller
Embedded sensors
Dynamic strain measurement
Damage detection
Acoustic emission
Piezoelectric sensors

ABSTRACT

Marine propellers made of fibre-reinforced composites have demonstrated the potential to outperform metallic propellers in terms of efficiency and under-water noise radiation. For full realisation of this potential in a tailored design process with realistic constraints, accurate information on the hydrodynamic loads acting on composite marine propellers and the structural integrity is of key importance. It is conceptualised that this information can be acquired without disturbing propeller hydrodynamics using a network of piezoelectric sensors embedded inside the blade. In this paper, feasibility of this concept has been investigated numerically and experimentally. Hydrodynamic loads on a composite propeller obtained from numerical simulations were used to assess the sensitivity of piezoelectric sensors in measuring the dynamic strain field due to the blade deformation. Subsequently, 25 small-scale carbon-epoxy composite samples were manufactured with embedded piezoelectric wafer sensors of different sizes, and subjected to non-destructive and destructive loading scenarios. Feasibility of measuring strains at different frequency ranges and damage-induced acoustic emissions was quantitatively assessed from these experiments. Furthermore, the influence of the embedded sensors on the ultimate strength and toughness of the specimens was investigated. It was found that at least 92% of the studied propeller blade would have dynamic strains measurable up to the first four harmonics by the considered piezoelectric sensors. In a four-point bending setup, it was additionally demonstrated that the embedded piezoelectric sensor captured damage-induced acoustic emissions up to specimen failure with an average signal to noise ratio of 17 dB. The results indicate that embedded piezoelectric sensor networks can have the capability to measure both low-frequency dynamic strains in composite marine propeller blades and damage-related acoustic emissions.

1. Introduction

Within the shipbuilding industry there is a widespread interest in the development of fibre-reinforced composite marine propellers. Compared to their metallic counterparts, composite propellers can have advantages such as improved efficiency, reduced underwater noise, smaller electromagnetic signature, and lower weight [1,2]. In order to assess and improve the design of composite marine propellers, measurement of the structural response have so far primarily been performed in cavitation tunnel, for example by Maljaars

---

* Corresponding author.
E-mail addresses: A.J.Huijer@tudelft.nl (A. Huijer), X.Zhang-6@tudelft.nl (X. Zhang), C.Kassapoglou@tudelft.nl (C. Kassapoglou), L.Pahlavan@tudelft.nl (L. Pahlavan).

https://doi.org/10.1016/j.marstruc.2022.103231
Received 13 January 2021; Received in revised form 2 November 2021; Accepted 16 April 2022
Available online 19 May 2022

et al. [3] and Garg et al. [4]. A notable progress is the work of Maljaars et al. [3] wherein a full-scale propeller, driving a ship in calm water, was monitored using Digital Image Correlation (DIC). However, open-water application of this method is hindered by the reduced visibility and increased scattering of light. Alternative measurement methods are highly desirable in this regard.

The layered nature of fibre-reinforced composite materials provides a unique opportunity to embed measurement devices such as Fibre-Bragg Gratings (FBG) and thin piezoelectric sensors [5–7]. Measurement of hydrodynamic loads, deformations, vibrations, and structural integrity with embedded sensors can lead to improvement in the design and assessment of future propellers, as well as in the maintenance of the in-service propeller.

Application of FBGs has shown promising outlook for strain and vibration measurement in composites. For embedding, FBGs are small in diameter and therefore their influence on the structural integrity of the host can be limited [8]. Seaver et al. [9] investigated measuring strains near the surface of a rotating carbon-fibre reinforced composite (CFRP) marine propeller in a water tunnel using FBGs. On stationary blades, progress is shown for alloy marine propeller blades [10], composite aeronautic propeller blades [11] and composite wind turbine blades [12]. Tian et al. [13] placed strain gauges on marine propeller models and were able to retrieve dynamic strains through a data acquisition system (DAQ) integrated in the hub. Zetterlind et al. [11] compared their FBG results to readouts of strain gauges placed on the blade and noted broad agreement between the two methods.

For more complex shapes, such as propeller blades, additional challenges with embedding optical fibres due to the large curvatures have been reported by Seaver et al. [14]. Also it is reported the directionality of FBGs might restrict guided wave capture [15]. With conventional strain gauges, the maximum recordable frequency is limited [16]. Piezoelectric sensors are a promising alternative. They can support a wider range of sampling frequencies [15], are less challenging to handle than optical fibres during the embedding process, and therefore are highly suitable for both dynamic strain measurement and ultrasonic-based structural health monitoring.

Song et al. [17] excited and measured guided waves using piezoelectric transducers to assess the structural health of rotating wind turbine blades. The piezoelectric sensors were embedded on and inside the blade. During a wind tunnel test and via a wireless DAQ the attenuating effect of damage on measuring excited guided waves was successfully detected. With thin piezoelectric polyvinylidene difluoride (PVDF) sensors, Sullivan and Mueller [18,19] measured aerodynamic pressures on an aluminium marine propeller and noted the need to correct the sensors for possible thermal effects in their application.

On small-scale coupon specimens, dynamic strain measurements using piezoelectric sensors were performed by Shin et al. [20] and Lin et al. [21] on vibrating composite specimens. In their research, experimental results were compared to analytic models to reconstruct dynamic strains. Their approach to model sensor response relies on predetermined strains, which is also the case in the works of Gopalakrishnan et al. [22] and Erturk et al. [23,24]. Ultrasonic elastic waves originating from fatigue damage have been passively recorded by Masmoudi et al. [25,26] in glass fibre specimens with piezoelectric sensors embedded inside. Multiple embedded sensors allow the localisation of damage, demonstrated by Dziendzikowski et al. [27], Yang et al. [28], Zamorano et al. [29] and Osmont et al. [30]. It should also be mentioned that piezoelectric sensors do not directly lend themselves for static strain measurement due to electrical discharge effects. Also, when embedding piezoelectric sensors, structural integrity of the composite is of concern since the sensor forms an inclusion between composite plies [25,27,28,31–38] or within plies [33–35,39], causing stress concentrations. In both glass-fibre reinforced plastics (GFRP) and CFRP specimens, the reported experimental results are case-specific due to variations in fibre lay-up, sensor geometry, insulation material (in the case of CFRP) and the type of loading applied. Therefore when other materials, lay-ups and loadings are considered, the effect on structural integrity is to be assessed.

Given the abovementioned advantages of piezoelectric wafer sensors in terms of embedding procedure and ability to measure at both low- and high-frequency regimes, they are believed to have great potential for application in composite marine propellers. This research aims to evaluate the feasibility of this concept with focus on measurement of strains and passive ultrasound. To the authors' knowledge, investigations with similar methods and application have not been published before. The ability of embedded piezoelectric sensors to measure dynamic strains acting on a real propeller blade is evaluated. The strain field is estimated from finite element simulation of a rotating composite marine propeller blade. An electro-mechanically-coupled model of the piezoelectric sensors has been constructed for translation of the input strain field to output voltage. Furthermore, coupon CFRP specimens with embedded piezoelectric sensors were designed and manufactured. These coupons are considered as the start of a step-by-step approach towards full-scale propeller assessment. The measured and modelled output voltage of the sensors are compared to load cell results and strain gauge results. To additionally evaluate the sensors effect on the composite structural integrity and to detect damage-related guided waves, the same specimens were subjected to four-point bending up to failure. The differences in flexural stiffness, strength, maximum strain and toughness of the specimens compared to specimens without sensors are presented. Also the amount and nature of damage-related guided waves recorded by the embedded sensor are compared to those recorded by surface-bonded piezoelectric sensors.

Regarding the organization of the paper, section 2 covers the modelling of a composite marine propeller blade in operation. Section 3 includes piezoelectric sensor modelling. In section 4 the experiments related to the dynamic strain measurements, damage-related guided waves, and structural integrity assessment are described. Results of the experiments and simulations are presented and discussed in section 5. The paper ends with conclusions and recommendations for the future work.

2. Modelling deformation of composite marine propellers

The dynamic behaviour of a composite marine propeller is simulated based on Maljaars et al. [2]. The deformation and strain behaviour is considered prospective for a flexible marine propeller, irrespective of fibre material. First the propeller material and geometry are described, followed by the load case and the method to retrieve a strain field.

2.1. Propeller description

The composite marine propeller presented and considered in this paper is a four-blade propeller with a diameter of 1 m. The blades are of sandwich construction and a section is shown in Fig. 1. Detailed specifics on the propeller blade may be found in Table 6.2 of the work of Maljaars [2]. The blade faces on the pressure and suction sides are made of composite laminates, and the core between the blade laminates is a polymat/resin rich material. The blade laminate consists of one ply of woven GFRP fabric and multiple unidirectional (UD) GFRP laminae. The woven fabric protects the blade surface against impact loads. The load carrying laminae consist out of E-glass fibres with a 600 gm^{-2} specific mass, infused with epoxy resin. Average lamina thickness is 0.5 mm. For the blade to attain a tapered thickness ply drops were introduced at regular intervals. It is considered that the strain behaviour of this propeller is representative for a typical flexible composite propeller blade, regardless of fibre material.

Elastic moduli E, Poisson ratios ν and shear moduli G of the isotropic core material, the woven GFRP fabric, and the UD GFRP lamina are listed in Table 1 [2]. The subscripts L, T and H in the elastic constants denote the longitudinal, the transverse and the thickness direction relative to the fibre direction, respectively.

2.2. Propeller load case

A non-uniform wake field is considered. The wake field is based on the Nautilus diving support vessel sailing a straight path in calm water at 10.4 knots (5.35 m/s) [2]. The propeller experiences the wake field with a rotational speed of 600 rpm.

2.3. Discretization and solving

A single blade is modelled using a finite element (FE) method with isotropic three-dimensional (3D) 20-node solid elements (type 21) for the core, and 3D 20-node composite brick elements (type 150) for the blade faces. The latter elements accommodate for the different fibre directions of the laminae and the varying amount of laminae. Marc/Mentat software was used for implementation of the model.

The different colours of the face element in Fig. 2 represent the different zones of the blade laminate, due to the regular ply drops, with the layups proposed by Maljaars [2]. For doubly curved composite structures, proper definition of material orientations is a key aspect in the modelling process [40]. A user-developed approach has been implemented to define the element-dependent (local) material orientations in the blade model (Fig. 3): direction 3 is the normal to the element surface tangent plane, direction 2 is the intersection between the element surface tangent plane and the (global) x-y plane, and direction 1 is therefore defined as the outer product of directions 1 and 2. In each ply of the blade laminates, the fibre orientation is defined as the angle with respect to direction 2 [41].

For spatial discretization of the entire blade, a mesh density of 29 × 30 × 4 was applied. As shown in Figs. 1 and 2, 29 elements were placed along the chord, 30 elements in radial direction, and 4 elements in through-thickness direction. In through-thickness direction, the outer elements represent the face sheets of the blade on pressure and suction side, while the inner two elements describe the core material. From the perspective of convergence it was shown that this mesh density can provide an accurate estimation [41]. Considering that the stiffness of the hub is much higher than the blade, the blade model is fully clamped at the blade-hub interface (Fig. 4). Note that at this stage, no piezoelectric sensors are modelled into this discretization. Hence potential changes in local stiffness in the blade due to the embedded piezoelectric sensor are not taken into account.

For temporal discretization, a full revolution of the propeller in the non-uniform wake field is divided into 60 time steps, and the fluid pressures have been computed for each step. Each pressure distribution snapshot was then transformed to nodal forces, and

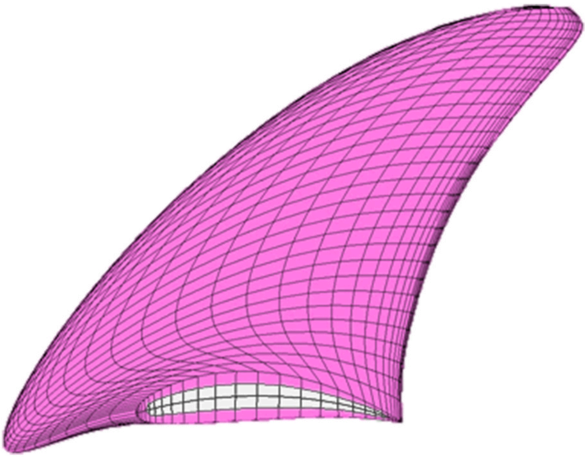

Fig. 1. Cross-section of the composite marine propeller blade: blade faces (magenta) and core (white).

Table 1
Elastic properties of the polymath/resin rich material, the woven GFRP fabric, and the UD GFRP lamina [2].

Elastic properties	polymat/resin rich material	woven GFRP fabric	UD GFRP lamina
E_L, E_T, E_H [MPa]	4000	21,584, 21,584, 3500	34,624, 5000, 3500
ν_{TL}, ν_{LH}, ν_{HT} [−]	0.3	0.192, 0.1, 0.1	0.0426, 0.1, 0.1
G_{TL}, G_{LH}, G_{HT} [MPa]	1538	3000, 2200, 2200	3100, 2200, 2200

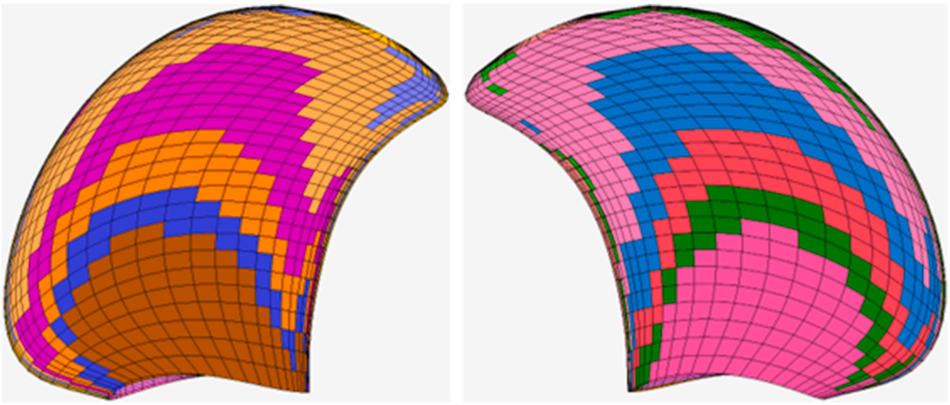

Fig. 2. The solid FE model of the composite blade: pressure side (left), suction side (right).

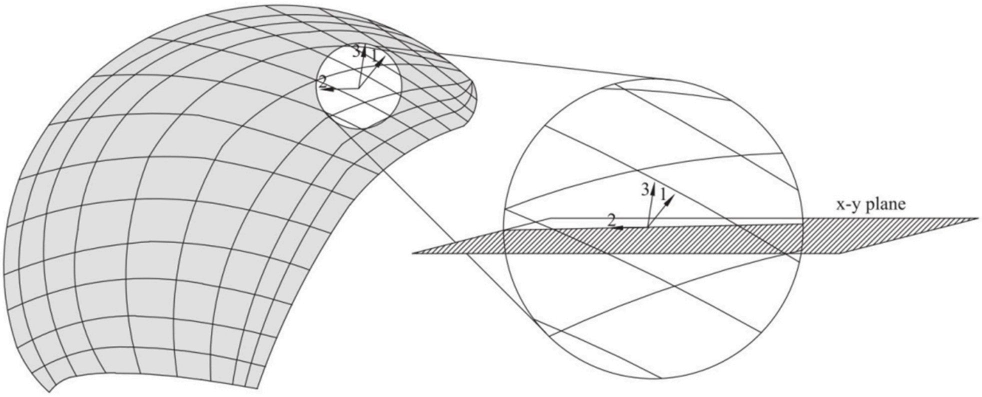

Fig. 3. Defining material orientations (Image taken from Ref. [2] with permission of the author).

applied to the centroid of elements at blade faces (Fig. 4). The resulting loads were employed in the FE analysis.

For every time step individually, a linear static analysis was performed. After solving, stresses were extracted for each ply at each time step. Using the stiffness matrix, these were converted to strains. The obtained strains were used in the feasibility analysis in the results.

3. Modelling piezoelectric sensor behaviour

The sensors considered in this research are piezoelectric wafers. In piezoelectric material, mechanical deformation of a crystal results in physical separation of positively-charged and negatively-charged parts. When a group of crystals are correctly structured, a macroscopic electric field is generated. Next to piezoelectric properties, the sensor material has elastic and dielectric properties as well. Taking these properties into account gives a set of constitutive equations, given in Eq. (1) [42]. Note that temperature effects (pyroelectricity) are neglected here.

$$\begin{aligned} \boldsymbol{S} &= \boldsymbol{s}^E \boldsymbol{T} + \boldsymbol{dE} \\ D &= \boldsymbol{d}^t T + \varepsilon E \end{aligned} \tag{1}$$

Here, $\boldsymbol{s}^E$ denotes the mechanical compliance matrix relating stress tensor $\boldsymbol{T}$ to strain tensor $\boldsymbol{S}$. Dielectric properties are represented

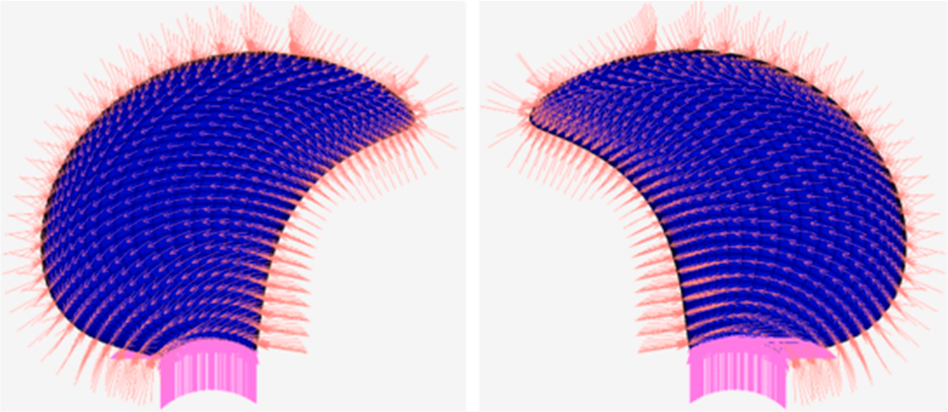

Fig. 4. The boundary condition and the loads: pressure side (left), suction side (right). The clamped boundary condition is given in pink, whereas the nodal loads are orange-coloured. The direction of the arrow implies the direction of the constraint and load. The length of the arrows is unitary and not related to load magnitude.

by $\boldsymbol{\varepsilon}$, relating electric field intensity $\boldsymbol{E}$ to electric flux intensity $\boldsymbol{D}$. Piezoelectric behaviour is modelled by $\boldsymbol{d}$ and $\boldsymbol{d}^t$ relating electric field intensity to strain and stress to electric flux intensity respectively. Full tensors in Voigt notation are used in the calculation. Material properties of the considered piezoelectric material are given in Table 2.

The performance of the sensor can be represented by the circuit laid out in Fig. 5 and obeys Kirchhoff's current law [23] given in Eq. (2).

Elements of this circuit are the piezoelectric sensor (with current I_s, Eq. (3)), an external capacitor and an external resistor (I_m, Eq. (4)), all placed in parallel to each other. The latter two indicate capacitive and resistive effects originating from wiring and the measurement device.

$$\sum I = 0 \rightarrow I_s + I_m = 0 \tag{2}$$

$$I_s = \frac{d}{dt}\int \boldsymbol{D} dA \rightarrow I_s = \frac{d}{dt}\int \left(\boldsymbol{d}^t \boldsymbol{s}^{E^{-1}}\boldsymbol{S} - \boldsymbol{d}^t \boldsymbol{s}^{E^{-1}}\boldsymbol{d}\boldsymbol{E} + \boldsymbol{\varepsilon}\boldsymbol{E}\right) dA \tag{3}$$

$$I_m = \frac{U}{R_m} + C_m\frac{dU}{dt} \tag{4}$$

In Eq. (3) electric flux density $\boldsymbol{D}$ is substituted by the piezoelectric constitutive relations from Eq. (1). Electrode surface area is defined by $\boldsymbol{A}$, in the form of $[0\ 0\ A_{el}]$ and $\frac{d}{dt}$ represents differentiation with respect to time. Electric field intensity is related to voltage U, assuming a linear distribution over sensor thickness h, through $\boldsymbol{E} = [E_1\ E_2\ U/h]^t$ [22]. Electrical resistance and capacitance are denoted by R_m and C_m respectively. Solving the differential equation resulting from Eq. (2), sensor voltage U can be recovered from a known strain field $\boldsymbol{S}$.

For low-frequency excitation, the terms dependent on a time derivative become relatively small compared to the resistance term. This leads to a leakage in voltage compared to the strain field amplitude and is known as electrical discharge [23,43]. In higher frequencies, electromechanical resonance occurs as well, which is linked to the integration of the strain field over the electrode area. With proper description of the strain field as a function of the driving voltage electromechanical resonance and antiresonance behaviour can be reproduced by the method presented [5].

3. Experiments

3.1. Manufacturing of test samples

It is anticipated that many future flexible marine propeller blades would be manufactured out of CFRP. Hence, twenty-five beam-

Table 2

Electromechanical, mechanical and electrical material properties of PZ27 piezoceramic. Taken from Ref. [44]. Permittivity ε_r^T is relative to the permittivity of vacuum and determined at zero stress T. Subscript 1 relates to both in-plane directions, while subscript 3 refers to the out-of-plane direction.

name	$\boldsymbol{d}_{31}, \boldsymbol{d}_{33}, \boldsymbol{d}_{15}$ [$\times 10^{-9}$ C/m]	$\boldsymbol{s}^E_{11}, \boldsymbol{s}^E_{12}, \boldsymbol{s}^E_{13}, \boldsymbol{s}^E_{33}, \boldsymbol{s}^E_{44=55}, \boldsymbol{s}^E_{66}$ [$\times 10^{-12}$ m^2/N]	$\boldsymbol{\varepsilon}^T_{11,r}, \boldsymbol{\varepsilon}^T_{33,r}$ [$\times 10^3$]
PZ27	−17,42.5,50.6	17, −6.6, −8.61, 23.2, 43.5, 47.1	1.8, 1.8

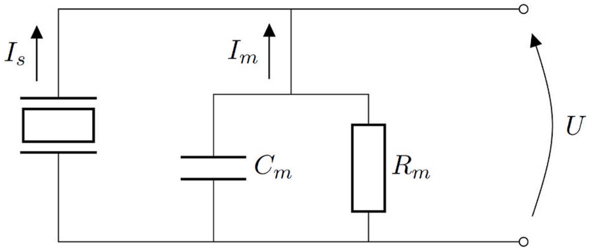

Fig. 5. Circuit representation of a piezoelectric sensor with current I_s and measurement system with current I_m.

Table 3
Specifics of the test samples produced.

Amount of specimens	Specimen name	Sensor material	Sensor diameter [mm]	Sensor thickness [mm]
12	s	PZ-27	7	0.24
6	L	PZ-27	20	0.29
7	N	–	–	–

shaped specimens were made out of this material. In twelve specimens, small sensors of 7 mm diameter and 0.24 mm thickness were embedded. Six specimens contained larger sensors, with a diameter and thickness of 20 mm and 0.29 mm. As a baseline, seven specimens did not host sensors. The number of specimens and sensor specifics are elaborated in Table 3. Views of the specimen and its manufacture are given in Figs. 6 and 7 [45,46].

The piezoelectric material used for the sensors were of the PZ-27 type, which has a depolarisation and maximum working temperature (350 ° C and 250° C) higher than the curing temperature of the host material (180° C) [44,47]. To achieve an omnidirectional sensitivity, the sensor was circular in shape. The thicknesses of 0.24 mm and 0.29 mm were chosen such that the host material would be affected minimally by the sensor's presence.

As the host material is electrically conductive, an insulation layer is applied between the piezoelectric sensor and the host. It is opted to use a thin layer of glass-fibre with epoxy resin (HexForce 00106 and Araldite LY 5052), following similar designs of [32,48]. The sensor was covered with insulation using a wet lay-up method, leading to a total thickness between 0.7 mm and 1.2 mm.

Bifilar enamelled copper wiring of 0.15 mm diameter was used, connected to an SMC connector to link the sensor to the data acquisition system. The sensor, wiring and connector were embedded parallel to the plane of the host material layers. The connector was further insulated using thin Kapton tape.

The host material was an AS4/8552 carbon fibre epoxy resin prepreg, laid-up in a $[[0,90]_7,0]_s$ symmetric cross-ply sequence. Resulting specimen thickness was 5.4 mm ± 0.1 mm. From the 20th to the 25th layer, up to five drop shaped cut-outs were made to accommodate sensors. This thickness location was considered representative for a future propeller blade. The sensors would not be placed inside the uppermost or lowest plies as any stress concentrations could have a detrimental effect on failure. However, when placed at the neutral axis, the piezoelectric sensor would not be able to measure linear bending behaviour. Placing the sensors at ¾ of the laminate thickness, or between the 20th and 25th plies of the 30 plies in total, is considered a representative trade-off.

Plies were cut from a roll with 150 mm width, giving square plates. The plates, with sensors and wiring embedded, were cured according to the manufacturers recommended procedure [47]. Afterwards, from these plates specimens were cut with a length of 150 mm and a width of 27 mm.

3.2. Description of experiments

Low-frequency strain measurements were performed by exciting the described specimens under four-point bending by means of a Zwick/Roell 1455 universal testing machine. Details of the set-up can be seen in Fig. 8 and Fig. 9. Piezoelectric sensor response, measured through a NI-USB6002 data acquisition system, was compared to the load measured by the testing machine itself, as well as by strain gauges (5 mm gauge length and 120.2 Ω resistance [49] connected to a Peekel Picas processing system) placed on the top and bottom of the specimens, at the location of the sensor. The load applied F_{LC} had a mean of 10.25 N, an amplitude of 9.75 N and was recorded using the load cell of the testing machine (Fig. 10). The loading generated a strain amplitude in the same order of magnitude as anticipated inside a propeller blade. For each specimen, the load was applied with three crosshead velocities v_m: 10 mm/min, 1 mm/min and 0.1 mm/min and with 20,20 and 5 cycles respectively. This approximately corresponds to 0.018 Hz, 0.18 Hz and 1.8 Hz respectively and is used to define a lower bound for measurable frequencies. The sample rate for the piezoelectric sensor was 100 Hz and no additional filters were applied.

To both measure damage-related acoustic emissions as well as to determine the influence of embedded sensors on flexural properties and mechanical strength of the specimen, the same bending set-up was used and the specimen was monotonically loaded up to failure (v_m =1 mm/min). Failure was defined as the moment the reaction force at each reaction point is less than half the maximum force encountered. To prevent local transverse matrix cracking at the loading pins, which was expected through analytical

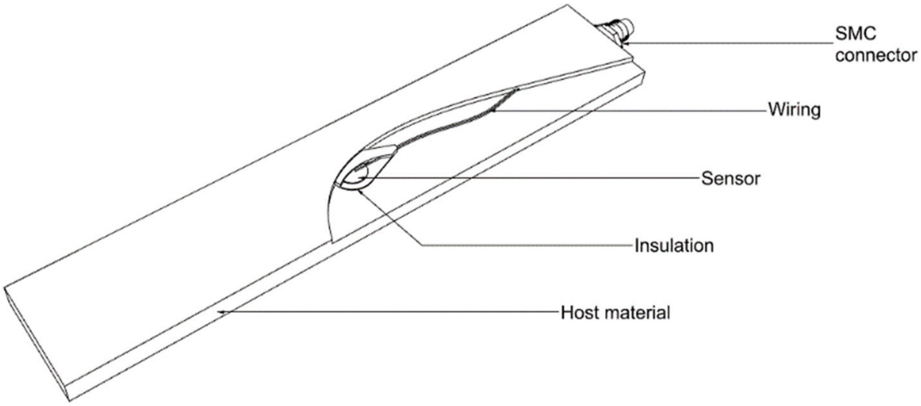

Fig. 6. Cut-through drawing of the test sample, showing different components.

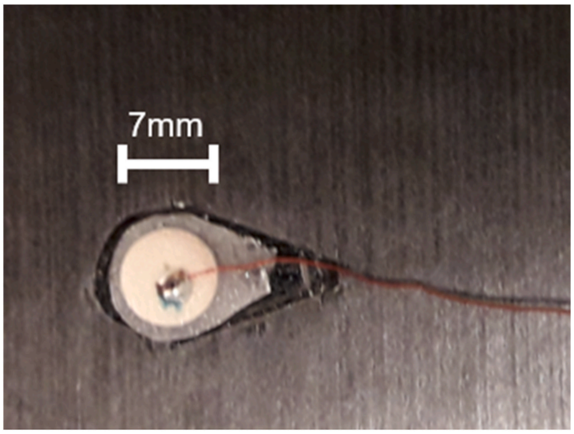

Fig. 7. The embedding of piezoelectric sensor 4s. Note the drop-shaped cut-out in the CFRP and the lighter coloured glass fibre insulation [46].

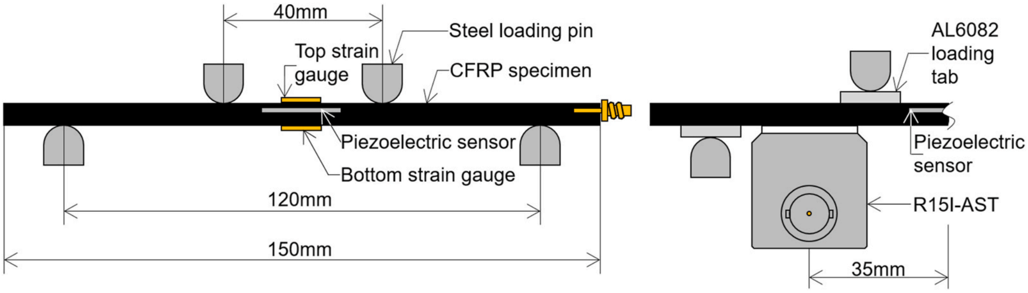

Fig. 8. Details of the four-point bending set-up, showing specimen, piezoelectric sensor on the compression side, strain gauges on top and bottom of the specimen and the loading pins. The left figure shows the set-up during low-frequency experiments, while the right figure shows (half of) the additions made for the destructive tests.

formulations [50] given the material properties [47], AL6082 tabs of 15 mm width and 3 mm thickness were placed between the specimen and the loading pins (steel ø10mm). The piezoelectric sensor read-out was amplified by 40 dB with a AEP5H preamplifier and connected to a Vallen AMSY6 data acquisition system. Furthermore, two commercial sensors, Mistras R15I-AST, were attached to the bottom side of the specimen, 35 mm away from the centre of the specimen, to compare results, as shown in Fig. 8. Signals were

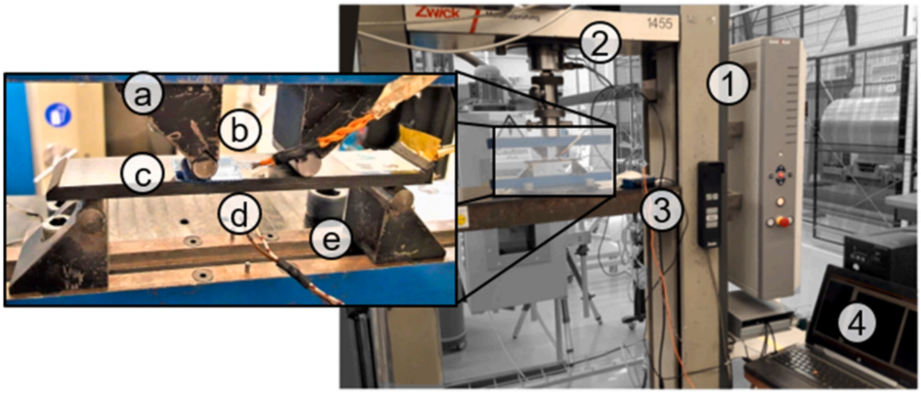

Fig. 9. General arrangement of the specimen in the testing machine during low-frequency data acquisition. Numbers 1 to 4 mark the Zwick/Roell 1455 universal testing machine, load cell, NI-USB6002 data acquisition system and the measurement laptop respectively. Letters 'a' to 'e' denote respectively a loading pin, the upper strain gauge location, lower strain gauge location and a support pin.

recorded when their amplitude exceeded a threshold set by the AMSY6 system. This threshold was set at 70 dB for the embedded sensor and 35 dB for the commercial sensors. Acquired signals were stored at a sampling rate of 10 MHz and included a pre trigger and post duration time of 200 μ s and 100μ s respectively. Signals were digitally filtered using a band pass filter to a domain of 20 kHz–960 kHz. In total, four baseline specimens were tested, together with two specimens with small sensors embedded on the compression side of the specimen, two specimens with large sensors on the compression side and two specimens with small sensors on the tension side.

4. Results

4.1. Feasibility of measuring dynamic strains on a propeller blade

As a case study the strains of a full propeller blade, derived in Section 2, were considered for the determining feasibility of measuring dynamic strains. Similarly, the geometry and material properties of the piezoelectric sensor used in experiments (Section 4) were adopted. Using the theory of Section 3 and the material properties of the sensor manufacturer [44], voltage amplitude $U(f,\mathbf{x})$ at frequency f and location $\mathbf{x}$ was obtained. Location $\mathbf{x}$ is based on the lamina closest to the core for both pressure and suction side of the blade. Each nodal location $\mathbf{x}$ is treated as to contain a piezoelectric sensor, with the size and properties equal to the 'small' sensor in the experiments (Table 2, Table 3). Strains acting in the nodal location are then regarded uniform over the sensor area.

A reference threshold amplitude U_{ref} is defined as 0.1 V, based on Wheeler et al. [51]. A feasibility index for measuring dynamic strains is introduced as follows (Eq. (5)):

$$FI_f(f,x) = \frac{|U(f,\mathbf{x})|}{|U_{\mathrm{ref}}|}. \tag{5}$$

Here, performing a measurement is considered feasible if $FI_f \geq 1$. No upper limit in voltage amplitude is introduced since it is expected issues with high voltage measurements can be mitigated with a proper design of a data acquisition system.

Ten periods, or 1 s, were modelled using the midpoint method to solve Eq. (2). A resistance of $R_m = 10^9\ \Omega$ was applied. No external capacitance C_m is applied. These values are representative for what was observed during the experiments described in Section 4.2. Resulting sensor voltages U for each location were evaluated for base frequency $f = 10$ Hz (established by the 600 rpm rotational speed) and its harmonics 20, 30, 40–50 Hz by means of a fast Fourier transform. The harmonics are assessed to provide a full view of the measurability of dynamic strains experienced by the propeller blade. Fig. 10 shows FI_f for the smaller sensor. For an overview of the coverage over the propeller blade, in Table 4 the percentage is given of evaluated locations that passed the failure criterion $FI_f \geq 1$.

The table shows that the base frequency is well captured, with a slight descend over the harmonics. The pressure side is better covered than the suction side, which can be attributed to higher strain magnitudes of the former respective to the latter. Analogous to the experimental observations, the larger sensor returns a higher coverage, which is due to the larger sensor thickness.

In Fig. 10 it is visible that particularly the tip of the propeller has a low feasibility index. The dominant strain components, being in-plane normal strain S_{xx} and S_{yy}, in this region are not of notably low magnitude but they appear of opposite sign. This local behaviour of compression in one direction and expansion in the other direction counteracts the build-up of voltage in the sensor, resulting in a relatively low feasibility index. In this context, it is relevant to note that the piezoelectric material (Table 2) has in-plane isotropic electromechanical properties.

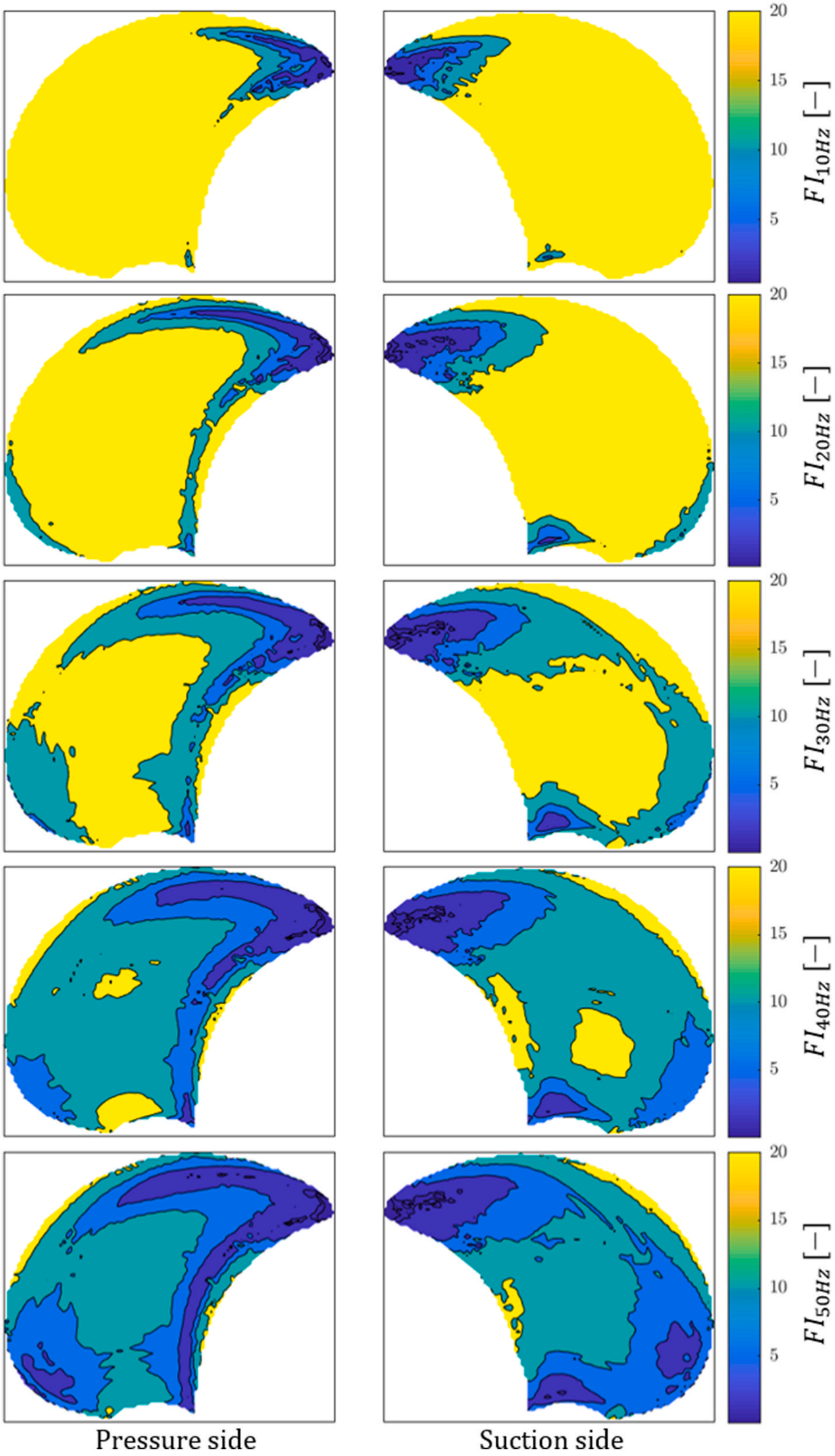

Fig. 10. Feasibility index for the smaller sensor on both the pressure and suction side of the marine propeller from 10, 20, 30,40–50 Hz from top to bottom. Note that the feasibility index is displayed from a value of one and is cut off at twenty.

Table 4
Coverage of the feasibility criterion over the propeller blade in per cents, for two types of sensors.

f [Hz]	Small sensor coverage [%]		Large sensor coverage [%]	
	Pressure side	Suction side	Pressure side	Suction side
10	98.7	98.3	99.1	98.8
20	96.7	94.3	96.9	95.0
30	96.1	93.5	96.5	94.1
40	95.4	92.6	95.8	93.3
50	94.5	92.1	95.3	93.2

Altogether, at least 92% of the propeller blade allows for dynamic strain measurement up to the fourth harmonic with sufficient quality, given the sensors used in the experiment.

4.2. *Experimental measurement of dynamic strains*

To evaluate the capability of the manufactured embedded piezoelectric sensors to measure low-frequency dynamic strains, as well as to compare measurements to the modelling presented in Section 3, low-frequency strains measurements were performed as described in Section 4. Results are shown here.

Out of 18 embedded piezoelectric sensors, 10 were able to detect low-frequency strains. Other sensors either were short-circuited or had a broken connection. The results for specimen 3 L, in terms of applied force F_{LC}, strain gauge strain S_{SG} and piezoelectric sensor output voltage U_{PZT} are given in Fig. 11 for $v_m = 10$ mm/min, 1 mm/min and 0.1 mm/min.

A number of observations are made from Fig. 11. Firstly, at higher crosshead velocities $v_m = 10$ mm/min and 1 mm/min, the applied load does not perfectly follow the imposed minimum and maximum of 0.5 N and 20 N. Secondly, the strain gauge results show instability, which is possibly due to the quarter Wheatstone bridge used [52]. Thirdly, with the piezoelectric sensor, the offset characterised by the other results decreases over time. Also, for $v_m = 0.1$ mm/min, the signal is more distorted and generally of a lower amplitude. These last three anomalies are related to electrical discharge, as described in Section 3.

To accurately compare sensors and results, the peak values (subscript $,a$) of the sensor voltage $U_{PZT,a}$ were divided by the peak values of the applied force $F_{LC,a}$ for each period. For a measure of comparison, the coefficient of variance is used. This is defined as the standard deviation of a dataset divided by its mean. When comparing results between different sensors, it turns out that for small sensors, the coefficient of variation of $U_{PZT,a}/F_{LC,a}$ for $v_m = 10$ mm/min, 1 mm/min and 0.1 mm/min is 25%, 21% and 42%. The corresponding coefficients of variation for large sensors are 14%, 14% and 19%, respectively. For analogy, the variation in specimen thickness alone would create a coefficient of variation of 1.6%, based on a quadratic relation between specimen thickness and $U_{PZT,a}/F_{LC,a}$. The seemingly-large coefficients of variation may firstly be attributed to local differences in embedding the sensor: Variation in the height location of the sensor, variation in glass-fibre insulation geometry and fibre-volume content and variation in cut-out size cause a variation in the strain field that is experience by the sensor. Secondly, variations in resistance and the small mean value of the

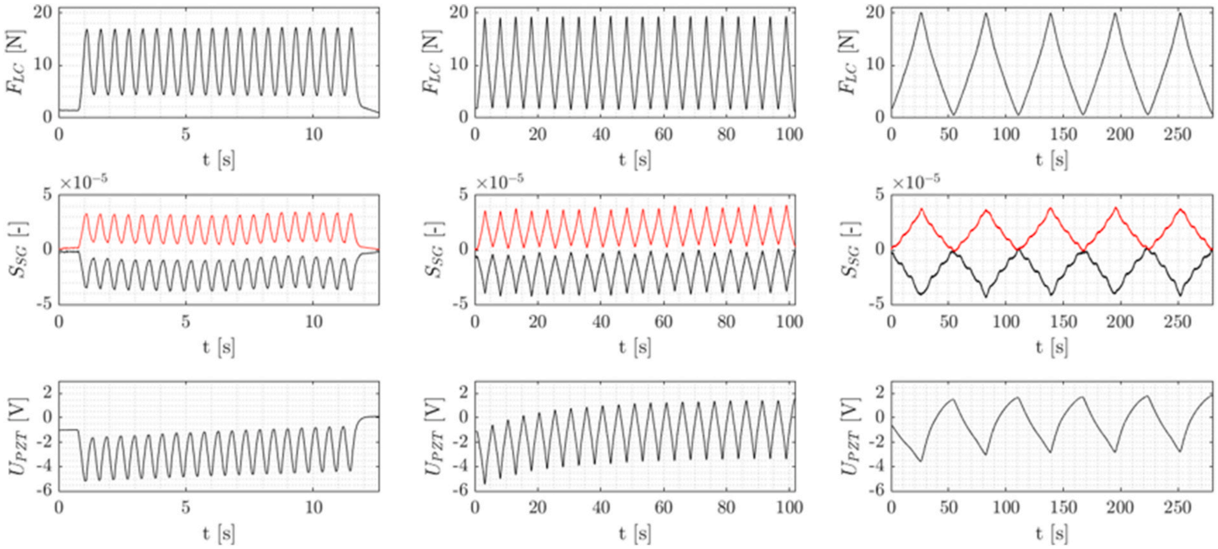

Fig. 11. Applied force F_{LC}, strain gauge read-out strain S_{SG} and piezoelectric sensor voltage U_{PZT} for $v_m = 10$ mm/min, 1 mm/min and 0.1 mm/min from left to right. In the strain gauge results, the black line denotes the topside strain gauge (in compression) and the red line gives the bottom-side strain result.

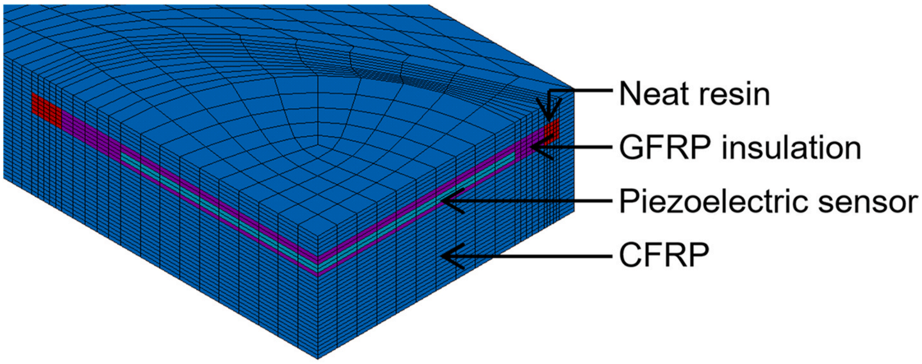

Fig. 12. Discretization of the sensor region for the larger embedded sensor. Note the circular shape of the sensor and the elliptical shapes of the glass insulation and neat resin.

Table 5
Elastic properties of the CFRP, sensor, insulation GFRP and neat resin, as used in the linear elastic modelling of the low-frequency experiment.

Elastic properties	CFRP AS4/8552 [47,53]	PZ 27 sensor [44,55]	GFRP insulation [54]	Neat resin [47,53]
E_L, E_T, E_H [GPa]	138.2, 9.8, 9.8	66, 66, 84	21, 21, 11.8	4.67
ν_{TL}, ν_{LH}, ν_{HT} [−]	0.35, 0.35, 0.4	0.389, 0.371, 0.371	0.17, 0.07, 0.07	0.35
G_{TL}, G_{LH}, G_{HT} [MPa]	4.1, 4.1, 1.96	41, 41, 41	3.5, 3.5, 3.5	1.73

output voltage at low velocities can be further sources of variation.

To simulate the strains encountered during the experiment, a 3D FEM model of a quarter of the specimen, including insulation, sensor and applied load was made in ANSYS [53]. Solid elements of type SOLID 186 and average length and thickness of 1 mm and 0.18 mm were used to model each lamina separately. To prevent skewing elements in thickness direction, all model thicknesses were chosen to match single or multiple lamina thicknesses. The small sensor was modelled with a thickness of one ply, whereas the large sensor had a two-ply thickness. The chosen thicknesses for the sensors closely approximate the values given in Table 3. The sensor was placed into five ply thicknesses of glass fibre. This corresponds to measured thicknesses from Section 4.1. The diameters of the small and large modelled sensors match exactly with the values in Table 3. Around the circumference of the sensor, the glass fibre insulation and a region of neat resin were modelled as elliptical in shape, each adding 1.5 mm and 3 mm in the width and length of the inset respectively. These dimensions may be compared to Fig. 7. A view of the discretised model is given in Fig. 12. The material properties were based on the data provided by Hexcel, Huntsman and Meggit [44,47,54,55] and are given in Table 5. The parameters related to the CFRP were updated to match the experimental results of the baseline specimens. More details on this approach may be found in Zhang et al. [53]. The Poisson's ratio and shear modulus of the GFRP were unknown and estimated. A load of 20 N was distributed over the contact location of the top loading pins. The lower support pins were modelled as a boundary condition allowing no deflection in the out-of-plane and transverse directions. A linear static analysis was performed. Fig. 13 shows the resulting strain in longitudinal direction (along the length of the specimen) for the larger sensor. Averaged over the sensor thickness and surface, values for the longitudinal strain were 16.5 μ m/m and 16.7 μ m/m for the small and large simulated sensor. Interpolating strain gauge measurements suggested a value of $\approx$ 20 μ m/m, which would be similar to the extreme value of what may be seen in Fig. 13.

The strains obtained on the sensor elements were averaged over the sensor thickness and subsequently used as input for the theory of Section 3, wherein the true sensor thickness and the material properties of the manufacturer [44] were applied. Evaluation of Eq. (2) gives a voltage signal dependent on the frequency of the applied load and resistance R_m in the system. Comparisons of experimentally-obtained $U_{PZT,a}/F_{LC,a}$ data to simulated results with $R_m = 10^8\ \Omega$ and $R_m = 10^{10}\ \Omega$ are shown in Fig. 14 for the small and large sensor respectively. From the loading velocity v_m, representative frequencies are derived and shown on the logarithmic axis of Fig. 14. Relative voltage amplitude U_(PZT,a)⁄F_(LC,a) is shown in boxplots for these frequencies. For low frequencies and low resistance R_m, voltage amplitude becomes low. For higher frequencies and higher resistance R_m, voltage amplitude reaches a constant value. In the experimental boxplots and the simulated lines alike, increase and stabilisation behaviour in voltage amplitude over frequency may be seen.

The absolute voltage values from the simulation are 40%–65% lower than the experimental values for the small and large sensors, respectively. It is considered that sources of variation can also be sources of this discrepancy. A discrepancy in material properties may occur between the experimental reality and the finite element model of the specimen. The material properties expected would be resin and glass fibre insulation stiffness and local CFRP stiffness. These discrepancies, in combination with differences in geometry of the cut-out and resin insulation and the height of the sensor location in the laminate may lead to an underestimation of the strains experienced by the sensor and will be the subject of further research.

5. Experimental measurement of damage-related guided waves

As described in Section 4, during failure testing, damage-related acoustic emissions were monitored by the embedded piezoelectric sensor in the specimen as well as by two attached R15I-AST sensors. With one specimen, the embedded piezoelectric sensor was able to record direct acoustic emissions, even up to the point of gross failure of the specimen. In Fig. 15 one of the signals of a damage-related acoustic emission is given, which are measured by both the embedded piezoelectric sensor (3 L, black) and the two commercial sensors (red and blue). In the figure the voltages U are corrected for their pre-amplification.

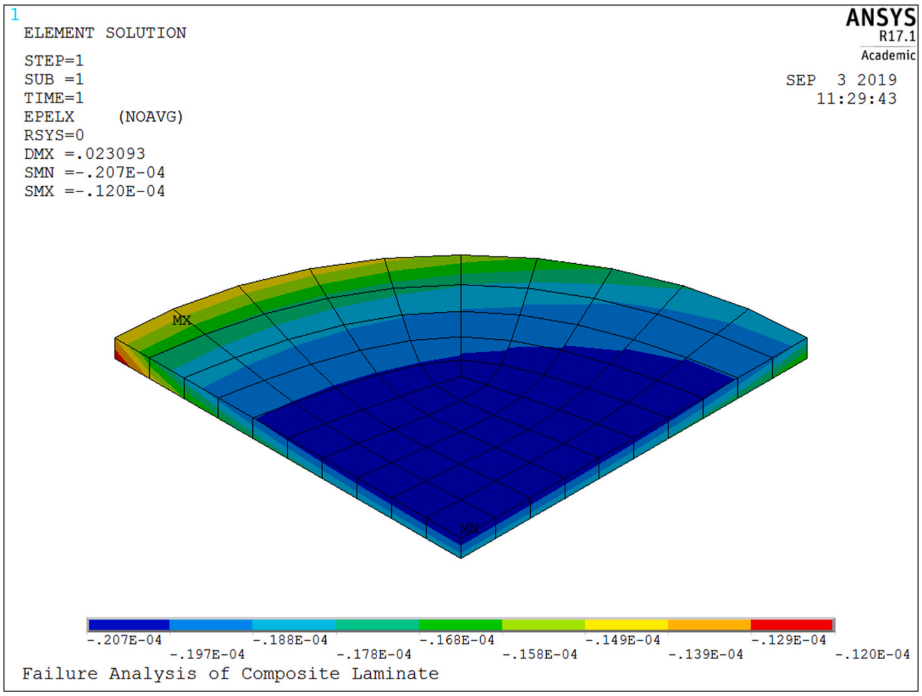

Fig. 13. Strain in longitudinal direction for the larger sensor at a load of 20 N on the specimen.

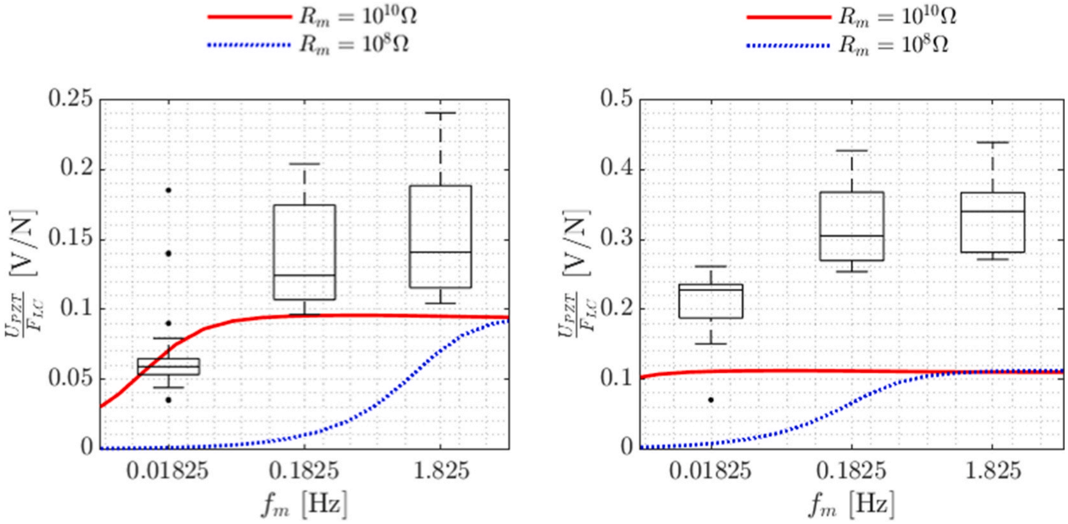

Fig. 14. $U_{PZT,a}/F_{LC,a}$ of the experimental results in the boxplot, the simulation is given in red for $R_m = 10^{10}\ \Omega$ and in blue for $R_m = 10^{8}\ \Omega$. The left figure shows the results for the small sensor, and the right figure shows results for the large sensor.

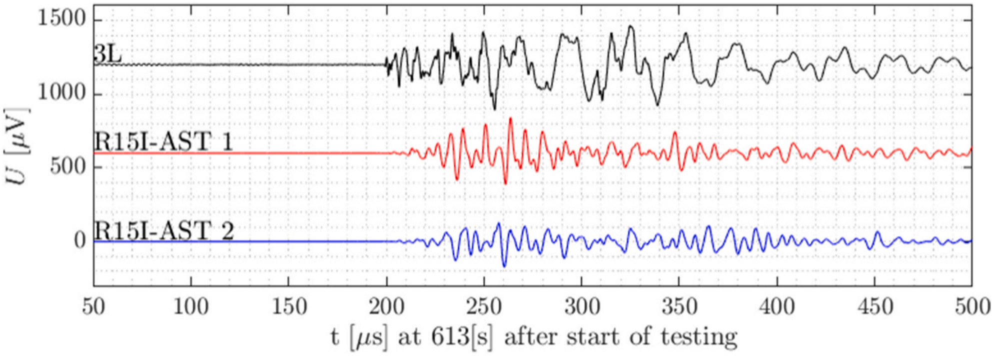

Fig. 15. Acoustic emission signal captured by all three sensors at time $t = 596$s since the start of the test [46].

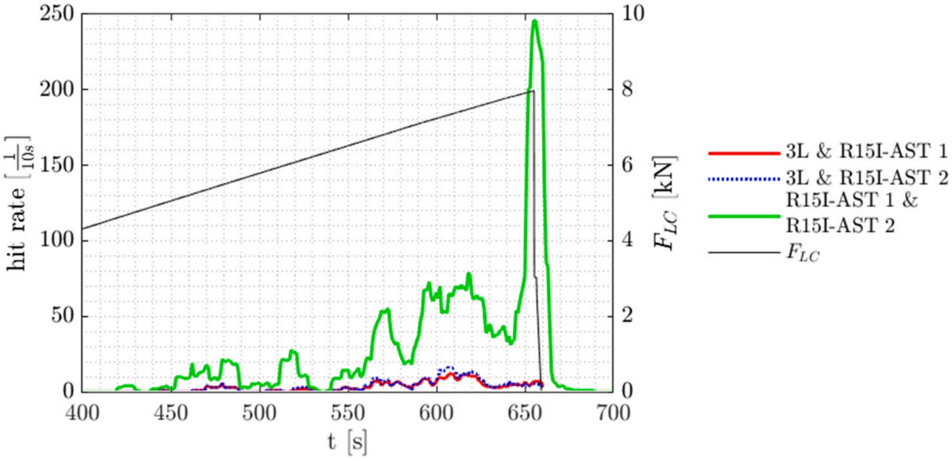

Fig. 16. Hit rate of signals measured by the embedded piezoelectric sensor (3 L) and a commercial sensor, and measured by both commercial sensors.

From the bulk of recorded signals, a hit rate analysis is defined, where the amount of signals recorded per sensor was accumulated in a window 5 s before and after a 1 s timestep. To remove bias from burst-type noise, only hits were taken into account that were measured near-simultaneously (within 10 μs) by at least two sensors. Results are shown relative to the applied load F_{LC} and for signals

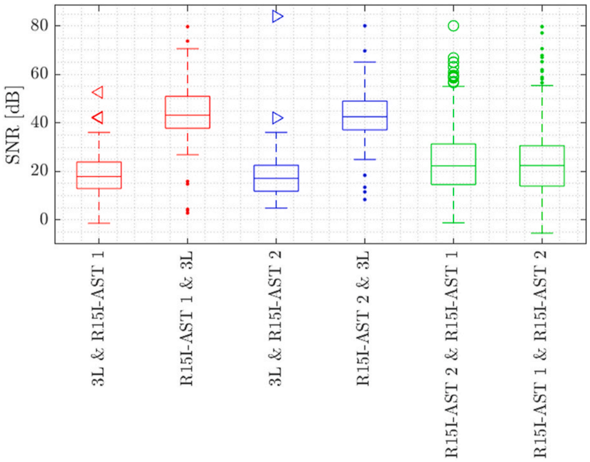

Fig. 17. Boxplots showing the SNR values captured by either both embedded piezoelectric sensor 3 L, in the first and third boxplots, and a commercial R15-AST sensor (second and fourth boxplot, red and blue for the two different commercial sensors) or by both commercial sensors, in green.

that were recorded by either the embedded piezoelectric sensor and at least a single commercial sensor (Fig. 16), or by at least the two commercial sensors. The hit rate of signals recorded by the embedded sensor is approximately an order of magnitude lower than the hit rate of the R15I-AST sensors. Nevertheless, it is visible that the trend in the rate of signals recorded by the embedded piezoelectric sensor is in line with that of the commercial sensors, up to around $F_{LC} = 7500$ N, after which the commercial sensors show a sudden increase in signals that is not covered by the embedded piezoelectric sensor. This might indicate a failure in the sensor or around the embedded sensor, blocking the propagation of elastic waves towards or through the sensor.

During the measurement of passive damage-related acoustic emissions, the transient signal is measured, as well as a pretrigger signal, being the reference signal acquired prior to the incoming of the acoustic emission. The signal to noise ratio *SNR* in dB, given in Eq. (6), is used as feasibility index FI_{AE} for measuring acoustic emissions.

$$FI_{AE} = SNR = 10\log_{10}\frac{\sum_{t_{signal}} U^2}{\sum_{t_{pretrigger}} U^2} \tag{6}$$

To demonstrate feasibility in measuring acoustic emissions, a minimum value of 1 dB is envisaged, based on comparable values from Horowitz et al. and Zhang et al. [56,57]. Fig. 17 shows boxplots of the SNR for signals captured by embedded sensor 3 L and by at least one of the commercial sensors. From these plots, it may be read the mean SNR of embedded sensor 3 L is at 17 dB, whereas the commercial sensors have a mean around 42 dB for the same hits. Hits that were captured by the commercial sensor but not necessarily by 3 L, show a mean SNR of 22 dB. This may be attributed to the lower threshold given to the commercial sensor compared to the embedded sensor. It can be said the embedded piezoelectric sensor 3 L is less sensitive than the commercial sensors. Nevertheless the SNR of the embedded piezoelectric sensor is considered sufficient, given the guideline of 1 db as described.

In a marine propeller in operation sources of ultrasonic elastic waves may not be limited to fatigue or failure related acoustic emissions. Cavitation implosion may create shock waves [58]. It is envisioned that readings from different source types have distinct waveform characteristics. In that situation, classification or clustering methods could be used to distinguish between cavitation-related ultrasonic waves and multiple types of damage-related acoustic emissions. These methods may use specific key parameters [26] or treat the waveform as a whole [46].

5.1. *Influence of embedding sensors on structural integrity*

In all specimens tested, failure was first noticed between $F_{LC} \approx 6000$ N and 7000 N at parts of the upper lamina, which was loaded in

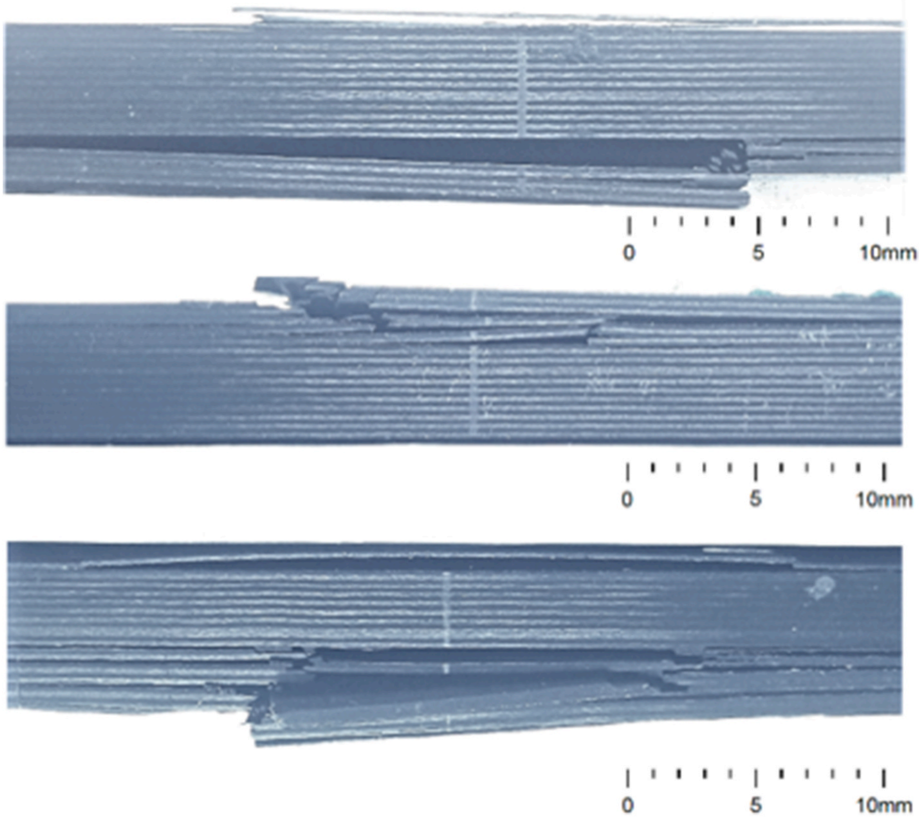

Fig. 18. Failed specimens, from top to bottom: 4 N, 2L, 5s(T) [46].

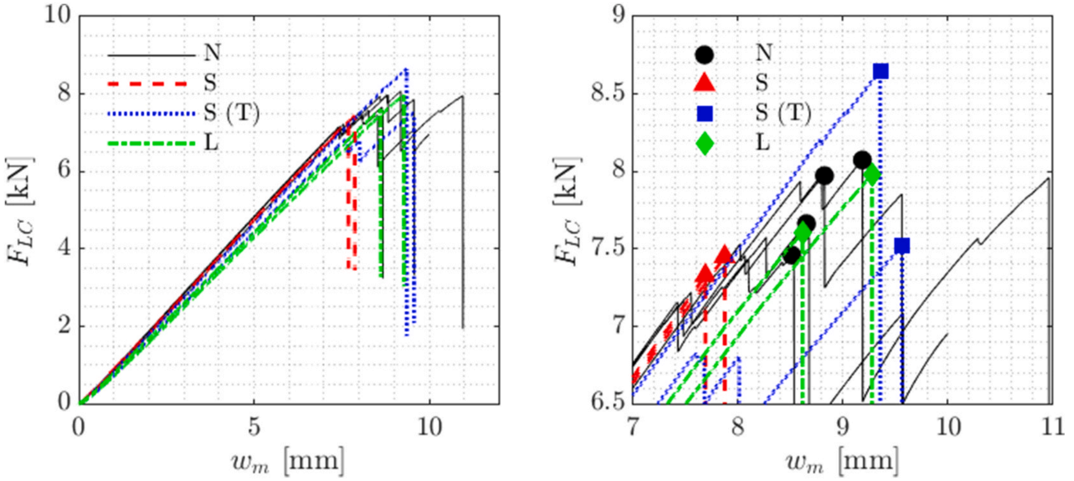

Fig. 19. Force-displacement results during failure testing. In the more focussed right figure, the markers indicate the maximum load resisted by the specimens.

Table 6
Stiffness, ultimate strain, strength and toughness, derived from the force-displacement data and specimen dimensions using ASTM D6272.

Specimen	1 N	2 N	4 N	7 N	2S	9S	4S(T)	5S(T)	2 L	3 L
E [GPa]	84.7	78.2	80.5	87.1	76.1	78.2	74.0	80.5	74.8	72.1
S_{max} [mm/m]	20.5	22.0	18.0	19.8	16.3	15.8	19.2	19.6	17.5	18.9
T [GPa]	1.19	1.16	1.12	1.10	1.10	1.09	1.28	1.12	1.16	1.21
W [MPa]	13.7	15.9	10.8	12.5	8.92	8.52	12.4	11.9	10.1	11.3

compression. Above $F_{LC} \approx 7000$ N, for baseline (N) specimens, the failure extended up to the four uppermost laminae and led to gross failure in one specimen. The other three baseline specimens experienced final tensile rupture, between 8 mm and 21 mm from the specimen centerline. Final tensile failure can be seen in the top photograph of Fig. 18 [46].

For specimens with sensors embedded in the compressive side the failure in the compressive upper laminae continued towards the cut-out laminae, typically near the interface between the sensor and glass fibre insulation or more towards the centre of the sensor (Fig. 18, middle picture).

Failure similar to the baseline specimens occurred for the specimens with sensors embedded on the tensile side, albeit 4.5 mm–8 mm from the centerline. This corresponds to failure through the sensor or through the insulating glass fibre (Fig. 18, bottom picture).

During the tests, both crosshead displacement w_m and load F_{LC} were monitored, giving the load-displacement data shown in Fig. 19. Based on these measurement data, specimen geometry and the procedure given by ASTM standard D6272 [59], specimen flexural stiffness E, maximum strain S_{max}, strength T and toughness W values were retrieved, given in Table 6. What stands out is that, on average, the stiffness of specimens with embedded sensors is 8% lower than their baseline counterparts, with an average of 6.6% for small sensors and 11% for large sensors. Ultimate strain dropped on average 11% (20% in small sensors on compressive side, 3.3% for small sensors on tensile side and 9.3% in large sensors) whereas flexural strength remained largely similar. Taking the entire load-displacement history into account, toughness decreased on average 20% due to embedding a sensor, with a 34% drop for small sensors on the compressive side, 8.1% in small sensors on the tensile side and 19% for large sensors. From these values, it seems embedding a piezoelectric sensor in the tensile side of a specimen loaded in bending is less damaging than when placed in the compressive side. The size of the sensor appears to be of minor influence, when placed in the compressive side. However it should be noted that the variation in the data is relatively large and the sample size is relatively small, making it premature to reach a general conclusion on the matter.

In application to the composite propeller, this preliminary data may hint towards further consideration on the locations inside the blade for the embedded sensors to be placed in view of structurally critical areas.

6. Conclusions

Feasibility of measuring dynamic strains and damage-induced ultrasound signals in composite marine propellers was investigated. By combining finite element simulation of a specific composite marine propeller in operation and electromechanically-coupled modelling of piezoelectric wafer sensors, the study suggests that 92% of the propeller blade area allows for measurements of dynamic strains with sufficient quality up to the fourth harmonic (50 Hz) of the blade using the considered embedded sensors.

It is furthermore confirmed experimentally that piezoelectric sensors embedded in a CFRP laminate are able to recover dynamic strains. With the set-up used, small-amplitude strains in the order of 20 $\mu\varepsilon$ were measured at frequencies as low as 0.018 Hz. Variation in signal amplitude between the utilized sensors was relatively large (14%–42%) and is mainly attributed to dissimilarities obtained during embedding. To be used in an independent dynamic strain measurement, an improvement in embedding procedure is considered for the future research.

In another experiment, damage-induced ultrasonic guided waves were successfully recorded using an embedded piezoelectric wafer sensor almost all the way up to final failure of the CFRP laminate. This was verified by comparison with two surface-bonded commercial sensors. The achieved signal-to-noise ratio of 17 dB shows the capability of the embedded sensor in recording the ultrasound guided-wave signals.

The influence of embedded piezoelectric sensors on the structural integrity of the CFRP laminate when loaded under four-point bending was preparatorily investigated as well. On average, the effect turned out to be limited to 3.3% drop in ultimate strain and 8.1% drop in toughness when the sensor was embedded on the tensile side. When embedded on the compressive side, ultimate strain and toughness were on average reduced further to ranges of 9.3%–20% and 19%–34% respectively, depending on the sensor size. It should be mentioned that the sample size demands further experimental research. The presented research may be seen as a preliminary work for the further development of self-sensing composite marine propellers using piezoelectric sensors. Topics of fatigue performance of the propeller, influence of the embedded sensor on full propeller flexibility and strength, preferred locations for the embedded sensors from a practical and structural perspective and measurement of cavitation damage with embedded sensors are considered as important next steps in this line of research.

Data availability

The raw/processed data required to reproduce these findings cannot be shared at this time as the data also forms part of an ongoing study.

Declaration of competing interest

The authors declare that they have no known competing financial interests or personal relationships that could have appeared to influence the work reported in this paper.

Acknowledgements

This work was supported by DMO Netherlands. The sponsors were sparsely involved in the study design but not in the collection, analysis and interpretation of data, nor in the writing of the report. The authors are also grateful to Andre Vaders and Pieter Maljaars for their valuable support and contribution.

References

[1] Koko TS, Shahin KO, Akpan UO, Norwood ME. Review of composite propeller developments and strategy for modeling composite propellers using PVAST. 2012.

[2] Maljaars PJ. Hydro-elastic analysis of flexible marine propellers. Delft University of Technology; 2019. https://doi.org/10.4233/uuid:19c9610b-9a72-42a6-8340-2ba01ec78cc6.

[3] Maljaars P, Bronswijk L, Windt J, Grasso N, Kaminski M. Experimental validation of fluid–structure interaction computations of flexible composite propellers in open water conditions using BEM-FEM and RANS-FEM methods. J Mar Sci Eng 2018;6. https://doi.org/10.3390/jmse6020051.

[4] Garg N, Pearce BW, Brandner PA, Phillips AW, Martins JRRA, Young YL. Experimental investigation of a hydrofoil designed via hydrostructural optimization. J Fluid Struct 2019;84:243–62. https://doi.org/10.1016/j.jfluidstructs.2018.10.010.

[5] Giurgiutiu V. Structural health monitoring with piezoelectric wafer active sensors. Academic Press; 2008.

[6] Frieden J, Cugnoni J, Botsis J, Gmür T, Corić D. High-speed internal strain measurements in composite structures under dynamic load using embedded FBG sensors. Compos Struct 2010;92:1905–12. https://doi.org/10.1016/j.compstruct.2010.01.007.

[7] Mieloszyk M, Majewska K, Ostachowicz W. Application of embedded fibre Bragg grating sensors for structural health monitoring of complex composite structures for marine applications. Mar Struct 2021;76:102903. https://doi.org/10.1016/j.marstruc.2020.102903.

[8] Mall S, Dosedel SB, Holl MW. The performance of graphite-epoxy composite with embedded optical fibers under compression. Smart Mater Struct 1996;5:209–15. https://doi.org/10.1088/0964-1726/5/2/009.

[9] Seaver M, Trickey ST, Nichols JM. Strain measurements from FBGs embedded in rotating composite propeller blades. Opt InfoBase Conf Pap 2006;1–4. https://doi.org/10.1364/ofs.2006.thd2.

[10] Javdani S, Fabian M, Carlton JS, Sun T, Grattan KTV. Underwater free-vibration analysis of full-scale marine propeller using a fiber bragg grating-based sensor system. IEEE Sensor J 2016;16:946–53. https://doi.org/10.1109/JSEN.2015.2490478.

[11] Zetterlind VE, Watkins SE, Spoltman MW. Fatigue testing of a composite propeller blade using fiber-optic strain sensors. IEEE Sensor J 2003;3:393–9. https://doi.org/10.1109/JSEN.2003.815795.

[12] Guo Z-S, Zhang J, Hu H, Guo X. Structural health monitoring of composite wind blades by fiber bragg grating. Int Conf Smart Mater Nanotechnol Eng 2007;6423:64230I. https://doi.org/10.1117/12.779233.

[13] Tian J, Croaker P, Zhang Z, Hua H. Dynamic strain measurements of marine propellers under non-uniform inflow. J Phys Conf Ser 2016;744. https://doi.org/10.1088/1742-6596/744/1/012094.

[14] Seaver M, Trickey ST, Nichols JM. Water tunnel tests of a composite propeller with embedded FBG. Conf. Proc. Soc. Exp. Mech. Ser., n.d.

[15] Kirkby E, de Oliveira R, Michaud V, Månson JA. Impact localisation with FBG for a self-healing carbon fibre composite structure. Compos Struct 2011;94:8–14. https://doi.org/10.1016/j.compstruct.2011.07.030.

[16] Ueda K, Umeda A. Dynamic response of strain gages up to 300 kHz. Exp Mech 1998;38:93–8. https://doi.org/10.1007/BF02321650.

[17] Song G, Li H, Gajic B, Zhou W, Chen P, Gu H. Wind turbine blade health monitoring with piezoceramic-based wireless sensor network. Int J Smart Nano Mater 2013;4:150–66. https://doi.org/10.1080/19475411.2013.836577.

[18] Sullivan CJ, Mueller TJ. Polyvinylidene fluoride film sensors for measurement of unsteady pressures on aerodynamic surfaces. Part I: design, fabrication, calibration and demonstration. Exp Fluid 1999. https://doi.org/10.1007/s003480050331.

[19] Sullivan CJ, Mueller TJ. Polyvinylidene fluoride film sensors for measurement of unsteady pressures on aerodynamic surfaces. Part II: application to a small-scale marine propeller in spatially distorted mean flow. Exp Fluid 1999. https://doi.org/10.1007/s003480050332.

[20] Shin S, Zamorano B, Elvin N. Comparison of the electromechanical properties of embedded and surface-mounted piezoelectric transducers. J Intell Mater Syst Struct 2016;27:2837–50. https://doi.org/10.1177/1045389X16642299.

[21] Lin B, Giurgiutiu V. Modeling and testing of PZT and PVDF piezoelectric wafer active sensors. Smart Mater Struct 2006;15:1085–93. https://doi.org/10.1088/0964-1726/15/4/022.

[22] Gopalakrishnan S, Ruzzene M, Hanagud S. Computational techniques for structural health monitoring. Springer London; 2011.

[23] Erturk A, Inman DJ. Piezoelectric energy harvesting. Wiley; 2011.

[24] Carrión JG, Frövel M, Pintado JM, Cabrerizo F. Extensive characterization of the intrusiveness of fibre bragg grating sensors embedded in a carbon fibre reinforced polymer. Proc 4th Eur Work Struct Heal Monit 2008:810–7.

[25] Masmoudi S, El Mahi A, Turki S. Fatigue behaviour and structural health monitoring by acoustic emission of E-glass/epoxy laminates with piezoelectric implant. Appl Acoust 2016;108:50–8. https://doi.org/10.1016/j.apacoust.2015.10.024.

[26] Masmoudi S, El Mahi A, Turki S, El Guerjouma R. Structural health monitoring of smart composite material by acoustic emission. In: d'Acoustique SF, editor. Acoust. 2012. Nantes, France; 2012.

[27] Dziendzikowski M, Kurnyta A, Dragan K, Klysz S, Leski A. In situ Barely Visible Impact Damage detection and localization for composite structures using surface mounted and embedded PZT transducers: a comparative study. Mech Syst Signal Process 2016;78:91–106. https://doi.org/10.1016/j.ymssp.2015.09.021.

[28] Yang B, Xuan F-Z, Jin P, Hu C, Xiao B, Li D, et al. Damage localization in composite laminates by building in PZT wafer transducers: a comparative study with surface-bonded PZT strategy. Adv Eng Mater 2018;21:1801040. https://doi.org/10.1002/adem.201801040.

[29] Zamorano-Senderos B, Elvin N. High-speed impact location detection on anisotropic composite panels using embedded piezoelectric sensors. J Intell Mater Syst Struct 2014;25:1921–36. https://doi.org/10.1177/1045389X13512188.

[30] Osmont DL, Dupont M, Gouyon R, Lemistre MB, Balageas DL. Piezoelectric transducer network for dual-mode (active/passive) detection, localization, and evaluation of impact damages in carbon/epoxy composite plates. In: Gobin PF, Friend CM, editors. Fifth Eur. Conf. Smart Struct. Mater. SPIE; 2000. https://doi.org/10.1117/12.396391.

[31] Tang H-Y, Winkelmann C, Lestari W, Saponara V La. Composite structural health monitoring through use of embedded PZT sensors. J Intell Mater Syst Struct 2011;22:739–55. https://doi.org/10.1177/1045389x11406303.

[32] Andreades C, Mahmoodi P, Ciampa F. Characterisation of smart CFRP composites with embedded PZT transducers for nonlinear ultrasonic applications. Compos Struct 2018;206:456–66. https://doi.org/10.1016/j.compstruct.2018.08.083.

[33] Chilles JS, Croxford A, Bond IP. Design of an embedded sensor, for improved structural performance. Smart Mater Struct 2015;24:115014. https://doi.org/10.1088/0964-1726/24/11/115014.

[34] Ghasemi-Nejhad MN, Russ R, Pourjalali S. Manufacturing and testing of active composite panels with embedded piezoelectric sensors and actuators. J Intell Mater Syst Struct 2005;16:319–33. https://doi.org/10.1177/1045389x05050103.

[35] Mall S. Integrity of graphite/epoxy laminate embedded with piezoelectric sensor/actuator under monotonic and fatigue loads. Smart Mater Struct 2002;11:527–33. https://doi.org/10.1088/0964-1726/11/4/307.

[36] Mall S, Coleman JM. Monotonic and fatigue loading behavior of quasi-isotropic graphite/epoxy laminate embedded with piezoelectric sensor. Smart Mater Struct 1998;7:822–32. https://doi.org/10.1088/0964-1726/7/6/010.

[37] Qing XP, Beard SJ, Kumar A, Ooi TK, Chang F-K. Built-in sensor network for structural health monitoring of composite structure. J Intell Mater Syst Struct 2006;18:39–49. https://doi.org/10.1177/1045389x06064353.

[38] Schulze R, Streit P, Fischer T, Tsapkolenko A, Heinrich M, Sborikas M, et al. Fiber-reinforced composite structures with embedded piezoelectric sensors. Proc. IEEE Sensors, vol. 2014– Decem, n.d., p. 1563–1566. https://doi.org/10.1109/ICSENS.2014.6985315.

[39] Lampani L, Sarasini F, Tirillò J, Gaudenzi P. Analysis of damage in composite laminates with embedded piezoelectric patches subjected to bending action. Compos Struct 2018;202:935–42. https://doi.org/10.1016/j.compstruct.2018.04.073.

[40] Chen J, Hallett S, Wisnom MR. Modelling complex geometry using solid finite element meshes with correct composite material orientations. Comput Struct 2010;88:602–9. https://doi.org/10.1016/j.compstruc.2010.02.004.

[41] Maljaars PJ, Kaminski ML, den Besten JH. Finite element modelling and model updating of small scale composite propellers. Compos Struct 2017;176:154–63. https://doi.org/10.1016/j.compstruct.2017.04.023.

[42] IEEE Standard on Piezoelectricity. ANSI/IEEE Std 176-1987 1988:0_1-. https://doi.org/10.1109/IEEESTD.1988.79638.

[43] Gautschi G. Piezoelectric sensorics: force strain pressure acceleration and acoustic emission sensors materials and amplifiers. Springer Berlin Heidelberg; 2006.

[44] Meggit. Data for modelling. 2017. https://www.meggittferroperm.com/resources/data-for-modelling/. [Accessed 10 April 2019].

[45] Huijer A. Load and damage measurements on fibre-reinforced composites with embedded piezoelectric sensors. 2019.

[46] Huijer A, Kassapoglou C, Pahlavan L. Acoustic emission monitoring of carbon fibre reinforced composites with embedded sensors for in - situ damage identification. 2021. Sensors (Switzerland).

[47] Hexcel corporation. HexPly 8552 epoxy matrix. 2016 (180C/356F curing matrix).

[48] Sala G, Olivier M, Bettini P, Sciacovelli D. Embedded piezoelectric sensors and actuators for control of active composite structures. Mech Therm Eng Dep Carlo Gavazzi Sp ESTEC. Eur Sp Agency; 2004.

[49] Kyowa strain gages KFGS-5-120-C1-11 2014.

[50] Young WC, Budynas RG, Sadegh AM. Roark's formulas for stress and strain. eighth ed. McGraw-Hill Education; 2011.

[51] Cm.: Pearson Wheeler AJ, Ganji AR, Krishnan VV. Upper saddle river SE - 480 blz. Introduction to engineering experimentation. LK. third ed. 2010. https://tudelft.on.worldcat.org/oclc/840427711.

[52] User manual PICAS [n.d].

[53] Zhang X. Short-term structural performance of self-monitoring composite marine propellers. Delft University of Technology; 2021. doi:10.4233/uuid:479b71c1-a006-4d9a-abda-b000a7711899.

[54] Huntsman. Araldite LY 5052/aradur 5052 COLD CURING EPOXY SYSTEMS. 2012.

[55] Meggit. Electronic correspondence with Karl Elkjaer [personal communication]. 2019.

[56] Horowitz SB, Mathias AD, Fox JR, Cortes JP, Sanghadasa M, Ashley P. Effects of scaling and geometry on the performance of piezoelectric microphones. Sensor Actuator A Phys 2012;185:24–32. https://doi.org/10.1016/j.sna.2012.07.008.

[57] Zhang L, Ozevin D, He D, Hardman W, Timmons A. A method to decompose the streamed acoustic emission signals for detecting embedded fatigue crack signals. Appl Sci 2017;8:7. https://doi.org/10.3390/app8010007.

[58] Tani G, Viviani M, Felli M, Lafeber FH, Lloyd T, Aktas B, et al. Noise measurements of a cavitating propeller in different facilities: results of the round robin test programme. Ocean Eng 2020;213:107599. https://doi.org/10.1016/j.oceaneng.2020.107599.

[59] D6272-17 A. Standard test method for flexural properties of unreinforced and reinforced plastics and electrical insulating materials by four-point bending. 2017.